

Research Paper

Biodegradable Core-shell Dual-Metal-Organic-Frameworks Nanotheranostic Agent for Multiple Imaging Guided Combination Cancer Therapy

Dongdong Wang^{1*}, Jiajia Zhou^{2*}, Ruohong Shi¹, Huihui Wu², Ruhui Chen¹, Beichen Duan¹, Guoliang Xia¹, Pengping Xu¹, Hui Wang³, Shu Zhou², Chengming Wang¹, Haibao Wang⁴✉, Zhen Guo²✉ and Qianwang Chen^{1, 3}✉

1. Hefei National Laboratory for Physical Sciences at Microscale, Department of Materials Science & Engineering & Collaborative Innovation Center of Suzhou Nano Science and Technology, University of Science and Technology of China, Hefei, 230026, China;
2. Anhui Key Laboratory for Cellular Dynamics and Chemical Biology, School of Life Sciences, University of Science and Technology of China, Hefei, 230027, China;
3. High Magnetic Field Laboratory, Hefei Institutes of Physical Science, Chinese Academy of Sciences, Hefei, 230031, China;
4. Radiology Department of the First Affiliated Hospital of Anhui Medical University, Hefei, 230022, China.

* Equal contribution to this study.

✉ Corresponding authors: Haibao Wang, E-mail: wanghaibao916@163.com; Zhen Guo, E-mail: zhenguo@ustc.edu.cn; Qianwang Chen, E-mail: cqw@ustc.edu.cn

© Ivyspring International Publisher. This is an open access article distributed under the terms of the Creative Commons Attribution (CC BY-NC) license (<https://creativecommons.org/licenses/by-nc/4.0/>). See <http://ivyspring.com/terms> for full terms and conditions.

Received: 2017.04.01; Accepted: 2017.09.29; Published: 2017.10.13

Abstract

Metal-organic-frameworks (MOFs) possess high porosity, large surface area, and tunable functionality are promising candidates for synchronous diagnosis and therapy in cancer treatment. Although large number of MOFs has been discovered, conventional MOF-based nanoplatfoms are mainly limited to the sole MOF source with sole functionality. In this study, surfactant modified Prussian blue (PB) core coated by compact ZIF-8 shell (core-shell dual-MOFs, CSD-MOFs) has been reported through a versatile stepwise approach. With Prussian blue as core, CSD-MOFs are able to serve as both magnetic resonance imaging (MRI) and fluorescence optical imaging (FOI) agents. We show that CSD-MOFs crystals loading the anticancer drug doxorubicin (DOX) are efficient pH and near-infrared (NIR) dual-stimuli responsive drug delivery vehicles. After the degradation of ZIF-8, simultaneous NIR irradiation to the inner PB MOFs continuously generate heat that kill cancer cells. Their efficacy on HeLa cancer cell lines is higher compared with the respective single treatment modality, achieving synergistic chemo-thermal therapy efficacy. *In vivo* results indicate that the anti-tumor efficacy of CSD-MOFs@DOX+NIR was 7.16 and 5.07 times enhanced compared to single chemo-therapy and single thermal-therapy respectively. Our strategy opens new possibilities to construct multifunctional theranostic systems through integration of two different MOFs.

Key words: MOFs, photothermal, chemotherapy, pH-responsive, NIR-responsive.

Introduction

Integrated nanotheranostic platform which provides comprehensive and efficient tools for real-time diagnosis has shown great promises in cargo delivery, image-guided therapy, and so on [1]. Chemotherapy, although is the most commonly used strategy, has suffered from limited treatment efficacy,

severe side effects and even the possibility of multidrug resistance [2, 3]. Recently, plenty of multifunctional nanoplatfoms that have the adaptability and responsiveness to various endogenous stimuli (e.g. pH [4], enzyme [5], and redox gradients [6]) or exogenous stimuli (e.g.

temperature [7], magnetic field [8], light [9]) have been designed to realize controllable cargo release for disease therapy and cell imaging. Photothermal therapy (PTT), which utilizes near-infrared (NIR) laser-induced thermal ablation of cancer cells has been widely explored and showed great combined therapeutic effects when applied together with common chemotherapy and other modalities [10-13]. Prussian blue (PB) has been approved by USA Food and Drug Administration (FDA) as a clinical medicine to reverse the damage of excess radiation [14]. Its perfect photothermal conversion effect originates from the charge transfer transition between Fe(II) and Fe(III) [15-17]. In our previous report, PB@MIL-100(Fe) nanocubes were prepared through layer-by-layer growth of MIL-100(Fe) shells for pH-responsive chemotherapy and PTT [18]. However Fe-containing compound administered parenterally can disturb the iron homeostasis and exhibit Fe-involved cytotoxicity via Fenton chemistry [19, 20]. Therefore, we have pressing need for the development of nanoparticles for combined cancer therapy with biocompatibility and high performances to satisfy the clinical requirements.

Personalized medicine applications should not only deliver target molecules to interesting locations in a controlled manner but provide the useful information of the size and location of tumors which is essential for operating optimal time window for therapy, and optimizing therapeutic efficacy. Owing to their excellent intrinsic properties, such as high porosity, large surface area, and tunable pore size, metal-organic-frameworks (MOFs) are widely used for gas separation and storage, catalysis, sensing, bioimaging and drug delivery [21-25]. Zeolitic imidazolate framework-8 (ZIF-8), which consists of Zn ions and 2-methylimidazolate (2-MeIM) linkers, is a potential carrier for anticancer drugs [26, 27]. ZIF-8 is nontoxic and biocompatible since the fact that zinc is the second most abundant transition metal in biology and that the imidazole group is integral to the amino acid, histidine [28, 29]. The coordination between zinc and imidazolate ions dissociates at pH 5.0-6.0 due to the effects of protonation [30, 31]. Thus it has exhibited desirable characteristic of rapid pH-sensitivity as a drug storage and delivery vehicle in acid tumor microenvironment (pH 5.7-7.8) while stay stable under normal physiological conditions [32, 33]. Recently, a number of imaging methods such as fluorescent [34], magnetic resonance imaging [35], and photoacoustic imaging [36], have been integrated to guide the planning of treatment. And the combination of fluorescence and MR imaging shows great promise in enhancement of precisely diagnosis [37-39].

Previous studies about combined chemo-thermal therapy are generally classified into two major strategies. One is directly connecting anticancer drug with photothermal agents, such as graphene and transition metal sulfide through chemical interaction or electrostatic adsorption [40-42]. Nevertheless, the loose attachment between drugs and carriers, potential long-term toxicity and limitation in multifunction hinder their further clinical application. The other one is the usage of hybrid compounds, such as mesoporous silica-coated gold nanorods and so on [43-45]. However, they still suffered from unsatisfactory release though mesoporous silica can improve the molecular loading and the efficacy of drug delivery. To solve these issues, we introduce heterogeneous hybridization as an effective methodology as it fuses the advantages of different materials and endows the hybrid materials with novel chemical and physiological properties. To the best of our knowledge, few works reported the combination of two MOFs for combined chemo-thermal therapy.

Herein, as a proof-of-concept for "Dual-MOFs", core-shell PB@ZIF-8 nanoparticle has been proposed for efficient multi-modal imaging guided synergistic chemo-thermal therapy (**Scheme 1**). Due to its distinctive core-shell dual-MOFs structure, it has shown a high doxorubicin (DOX) loading capacity (857.32 mg g⁻¹). We demonstrate that CSD-MOFs@DOX is a promising pH (endogenous) and NIR (exogenous) dual-stimuli responsive drug delivery system. We believe that a new avenue may be found for potential diagnostic application in cancer therapy through combination of two MOFs with different functionalities. Furthermore, the CSD-MOFs@DOX show improved therapeutic efficiency both *in vitro* and *in vivo*. With more study in the future, a versatile synthetic strategy is expected for synthesizing other biocompatible MOFs encapsulated photothermal agents.

Results and Discussions

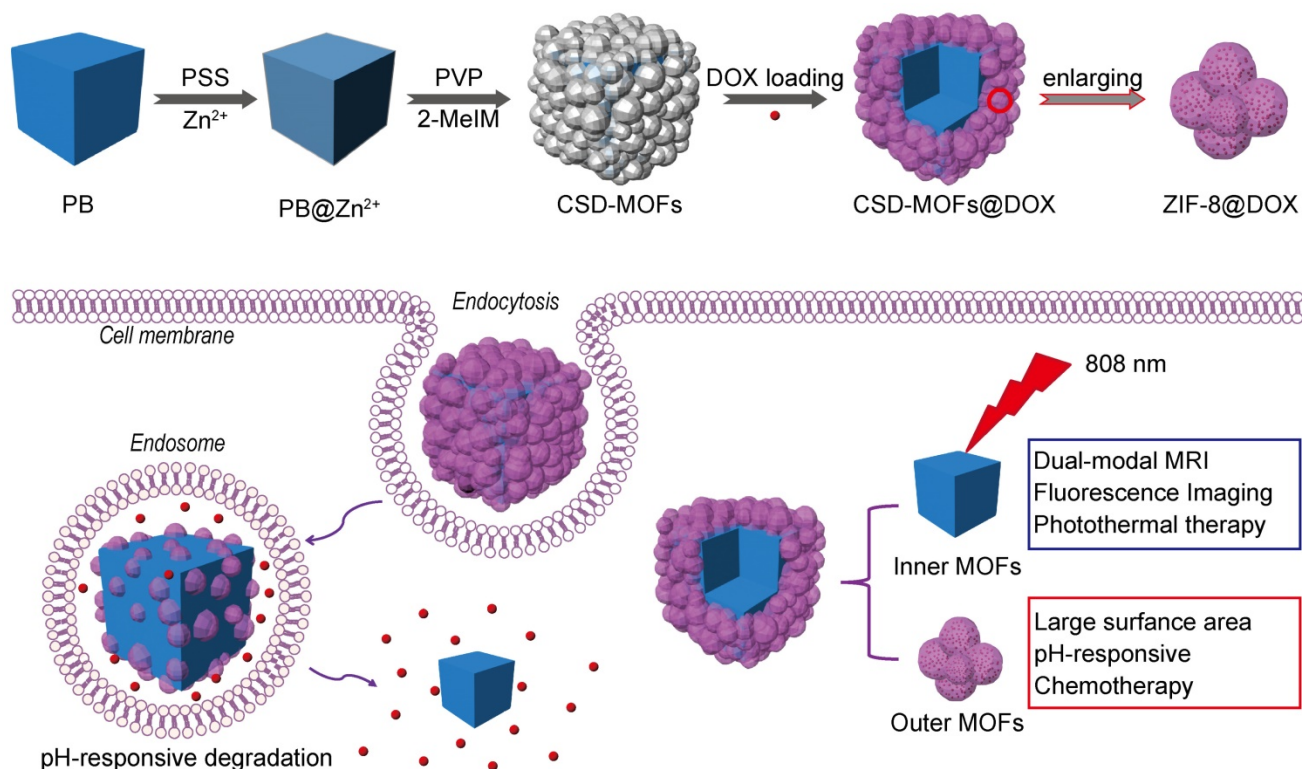
In this work, PB nanocubes were synthesized according to previous literature with modifications [18]. Scanning and transmission electron microscopy (SEM and TEM) results showed that the average diameter of the prepared PB is around 100 nm (**Figure 1a**, **Supplementary Figure S1**) which is slightly smaller than the results from Dynamic light scattering (DLS) measurements (**Figure 1f**). Later, PB was modified with Poly(sodium-4-styrenesulfonate) (PSS) molecules to form electronegative surface. Zn²⁺ cations are then attracted onto the negatively charged surfaces for the growth of ZIF-8 shell. The yielded CSD-MOFs showed a uniform ZIF-8 shell of 20 nm (**Figure 1b**, **1c**). High-angle annular dark-field

scanning transmission electron microscopy (HAADF-STEM) and elemental mapping were conducted to confirm the core-shell nanostructures (**Figure 1d**). The elements C and N are homogeneously distributed throughout the whole nanostructures while Fe and Zn are in the core and shell, respectively. Additionally, the element line mapping and EDS analysis also gives the compositional and structural details, indicating ZIF-8 has been successfully coated onto PB to form the core-shell structure (**Supplementary Figure S2, S3**). Inductively coupled plasma mass spectroscopy (ICP-MS) analysis showed that the molar ratios of Fe/Zn is 5.01/1 which is slightly higher than 4.89/1 based on EDS analysis. The weight ratio of PB/ZIF-8 in CSD-MOFs was estimated to be 70.4/29.6 according to thermogravimetric analysis (**Supplementary Figure S4**).

The XRD result showed two sets of characteristic peaks indicating that the products consist of ZIF-8 and PB crystals (**Figure 1e**). Fourier transform infrared spectroscopy (FT-IR) spectrum of pure 2-MeIM showed absorption peak at 1843 cm^{-1} (N-H stretching vibrations) and broad band ranging from 2200 cm^{-1} to 3300 cm^{-1} (N-H...N hydrogen bond) (**Supplementary Figure S5**) [46]. Compared to pure 2-methylimidazole, disappearance of the above absorption bands indicates the successful formation of ZIF-8 structure (**Figure 1g**). The C-N absorption bands

from outer ZIF-8 were found in the $1100\text{--}1400\text{ cm}^{-1}$ region. Moreover, absorption peak at 422 cm^{-1} confirms the successful coordination between Zn and N [47]. The stretching band (C≡N) of PB can be found at 2090 cm^{-1} .

A series of comparative experiments have been performed to study the influence of possible conditions on the morphology. The samples showed regular core-shell structure with 0.02, 0.04 or 0.08 g PVP as surfactant (**Figure 2b-d**). However the product without PVP showed irregular ZIF-8 agglomeration (**Figure 2a**). This indicates PVP can prevent agglomeration and contribute uniformed ZIF-8 shell. The amphiphilic PVP adsorbed on surfaces of PB will be hydrated and a bigger hydration shell will thus be formed, therefore sterically preventing agglomeration and stabilizing the composite particles. Besides, PVP consists of a highly polar amide group within the pyrrolidone ring and apolar alkyl chain, which will provide the nanoparticles with an enhanced affinity to ZIF-8 nanocrystal nucleus. To further investigate the rapid growth ratio of ZIF-8, products after reaction for 6, 8, 21, and 48 h were collected. No obvious differences of morphology of ZIF-8 were obvious as shown in SEM images (**Figure 2e-h**). During the synthesis, we found that the color of the mixture turn from blue to light blue within 5 min after the addition of precursor agents, which suggest the fast nucleation of ZIF-8 on the PB surface.



Scheme 1. (a) Schematic illustration of synthetic procedure of CSD-MOFs and (b) schematic representation: CSD-MOFs@DOX as an effective multi-modal therapeutic agents for synergistic tumor therapy.

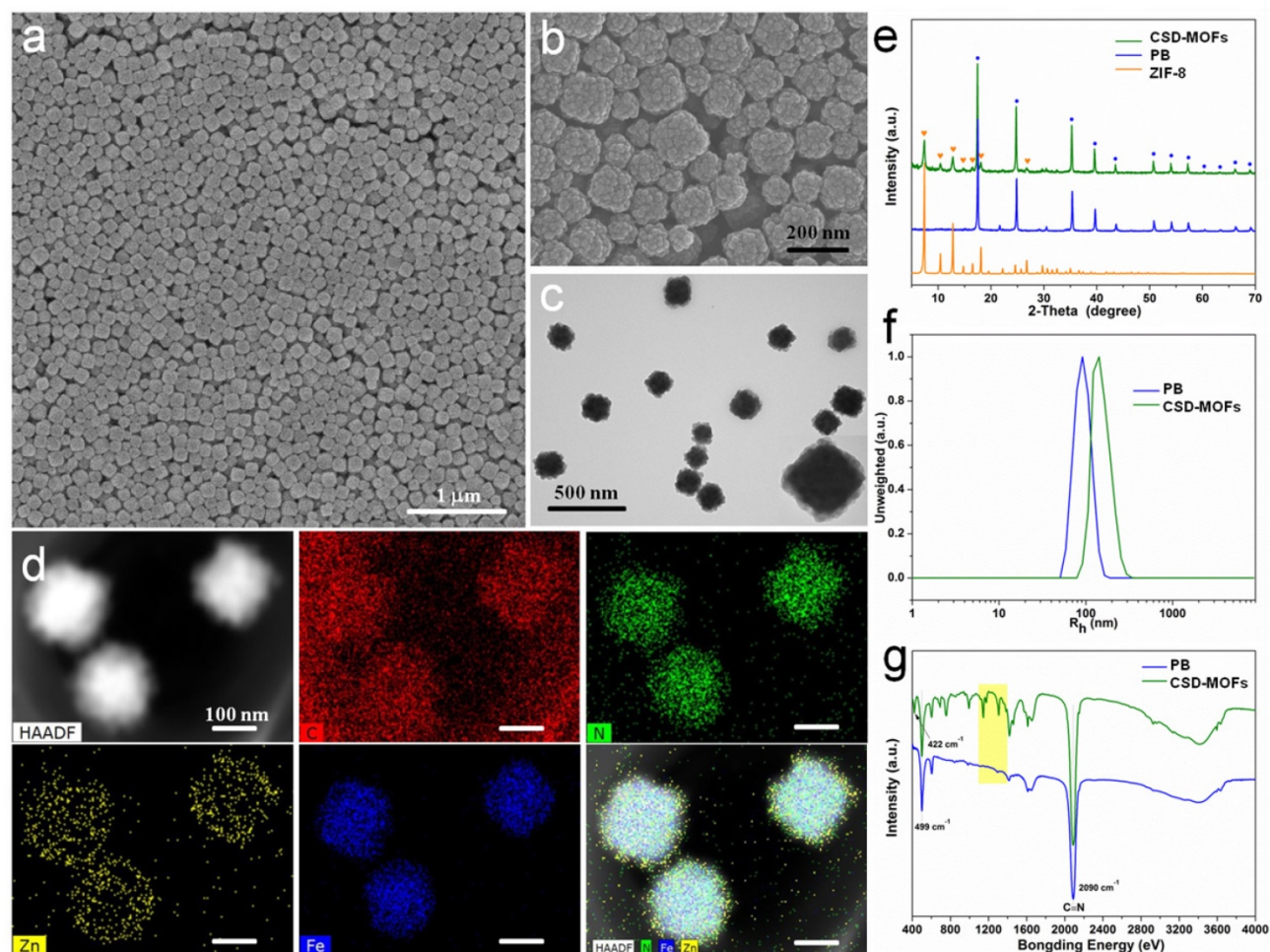


Figure 1. Characterization of as-prepared CSD-MOFs particles. SEM images of (a) PB and (b) CSD-MOFs nanoparticles. (c) TEM images of CSD-MOFs nanoparticles. The insets in (c) is TEM image of a single CSD-MOFs at a higher magnification. (d) HAADF-STEM image and EDX elemental mapping of core-shell CSD-MOFs nanostructure. (All scale bars are 100 nm). (e) XRD pattern of CSD-MOFs, PB and ZIF-8. (f) Dynamic Light Scattering measurement and (g) FTIR spectra of PB and CSD-MOFs.

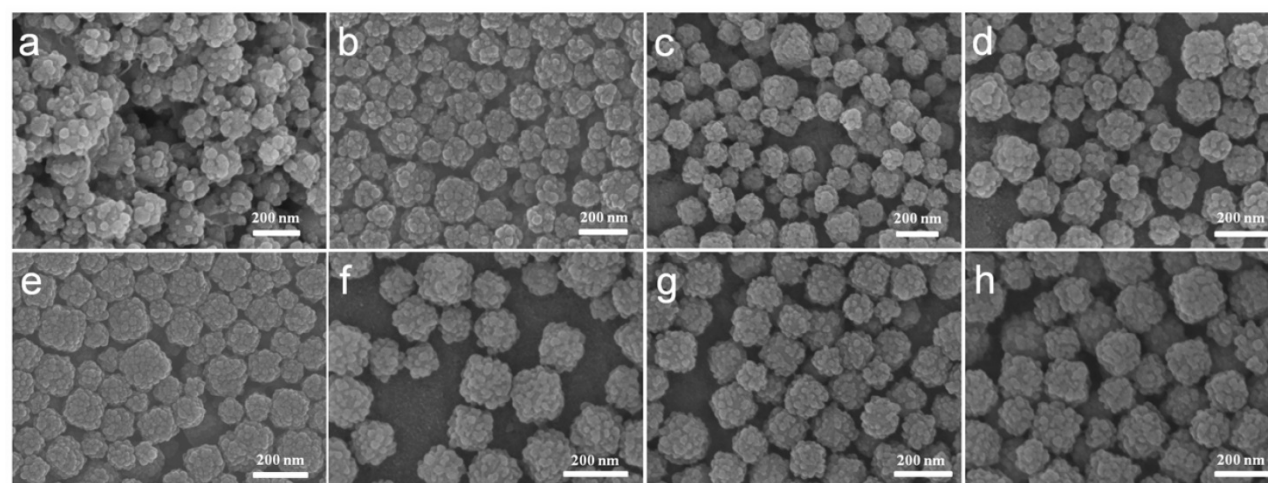


Figure 2. (a-d) SEM images of CSD-MOFs with 0 g, 0.02 g, 0.04 g, and 0.08 g PVP as surfactant, respectively. And (e-h) SEM images of CSD-MOFs with reaction time of 6 h, 8 h, 21 h, and 48 h, respectively.

Next, the effect of concentrations of precursors on the synthesis of ZIF-8 shell could shed light on its formation mechanism. Well-defined core-shell morphology can be observed when the concentration

of Zn^{2+} is 0.043 M (Figure 3a, 3d). In addition, no isolated ZIF-8 nanoparticles are presented, demonstrating that the growth of ZIF-8 is strictly limited to the surfaces of PB nanoparticles. While with

concentration of Zn^{2+} increasing from 0.043 to 0.086 M, the product comprised not only desired core-shell structures but other undesired freestanding ZIF-8 nanoparticle (Figure 3b, 3e). Moreover, when the initial concentration of Zn^{2+} was simultaneously increased to 0.172 M, no ZIF-8 was coated on the surface of PB cubes and only independent irregular small ZIF-8 crystals presented (Figure 3c, 3f). The isolated and coated ZIF-8 particles are dominated by homogeneous nucleation and heterogeneous nucleation, respectively. Herein, at low precursors concentrations, the nanoparticle-induced heterogeneous nucleation takes place easily than homogeneous nucleation due to the lower required energy barrier. In this way, small ZIF-8 crystal nucleus will first form on the surface of PB nanocubes, thus leading to uniform ZIF-8 shells. However, at higher concentrations, homogeneous nucleation competes with heterogeneous nucleation, so isolated and coated ZIF-8 particles will co-exist. When the concentration exceed the critical concentration, independent irregular small ZIF-8 crystals are formed through the homogeneous nucleation mechanism.

The Brunauer-Emmett-Teller (BET) surface area and pore size distribution indicated that the CSD-MOFs possess both mesopores and micropores (Supplementary Figure S6). The micropores should be originated from aggregation of small ZIF-8 crystals. The BET surface area of CSD-MOFs increased from $52.19 \text{ m}^2 \text{ g}^{-1}$ to $191.81 \text{ m}^2 \text{ g}^{-1}$ compared with pure PB. In addition, CSD-MOFs nanocubes presented a large pore volume of $0.182 \text{ cm}^3 \text{ g}^{-1}$. DOX was chosen as a drug model with a high loading capacity (852.3 mg g^{-1}) and high efficiency (85.23%). The amount of DOX

was estimated considering the weight losses (828.2 mg g^{-1}) which is slightly lower than the value based on UV-vis data (Supplementary Figure S7). Herein, the high DOX loading capacity should be attributed to not only the interactions between DOX and inner PB together with outer ZIF-8 but the unique microstructure of outer ZIF-8. The interactions included coordinative bonding between chemical groups (e.g., amino and carbonyl) of DOX and inner Fe(III). Besides, π - π stacking between the aromatic anthracycline of DOX and the $-C\equiv N$ - pore walls of PB also contributed loading capacity [48]. UV-vis-NIR spectroscopy also showed red shift of DOX and PB in CSD-MOFs@DOX compared to pure DOX and pure PB (Figure 4a). Additionally, the gaps between small ZIF-8 crystals also contributed to the high loading capacity. Subsequently, the photothermal conversion ability was investigated. PB and CSD-MOFs aqueous solutions with different concentrations were separately exposed to an 808 nm laser (1.6 W cm^{-2} , 5 min). The blank test demonstrated that the temperature of pure water was only increased by 3°C . With the addition of PB and CSD-MOFs, the temperature increases dramatically with the increase of the irradiation time (Figure 4b, Supplementary Figure S8). Additionally, the photothermal conversion efficiency (η) of CSD-MOFs was calculated to be 23% (Supplementary Figure S9). The temperature change during laser irradiation was recorded with an infrared (IR) thermal camera (Figure 4c). Besides, the CSD-MOFs showed almost the same absorbance and negligible morphology change from TEM images, indicating its remarkable photo-stability (Figure 4d, Supplementary Figure S10).

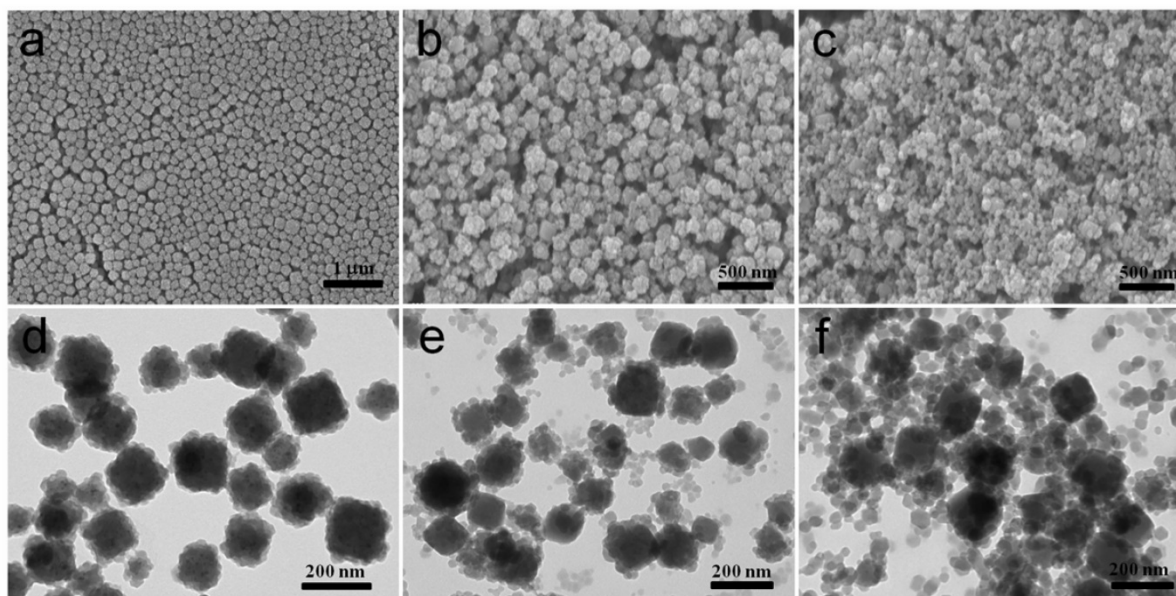


Figure 3. Representative SEM (a-c) and TEM (d-f) images of CSD-MOFs with initial Zn^{2+} concentration of 0.043 M, 0.086 M, and 0.172M respectively (PVP is 0.04 g, reaction time is 6 h, mole ratio of 2-MeIm/ Zn^{2+} is 4).

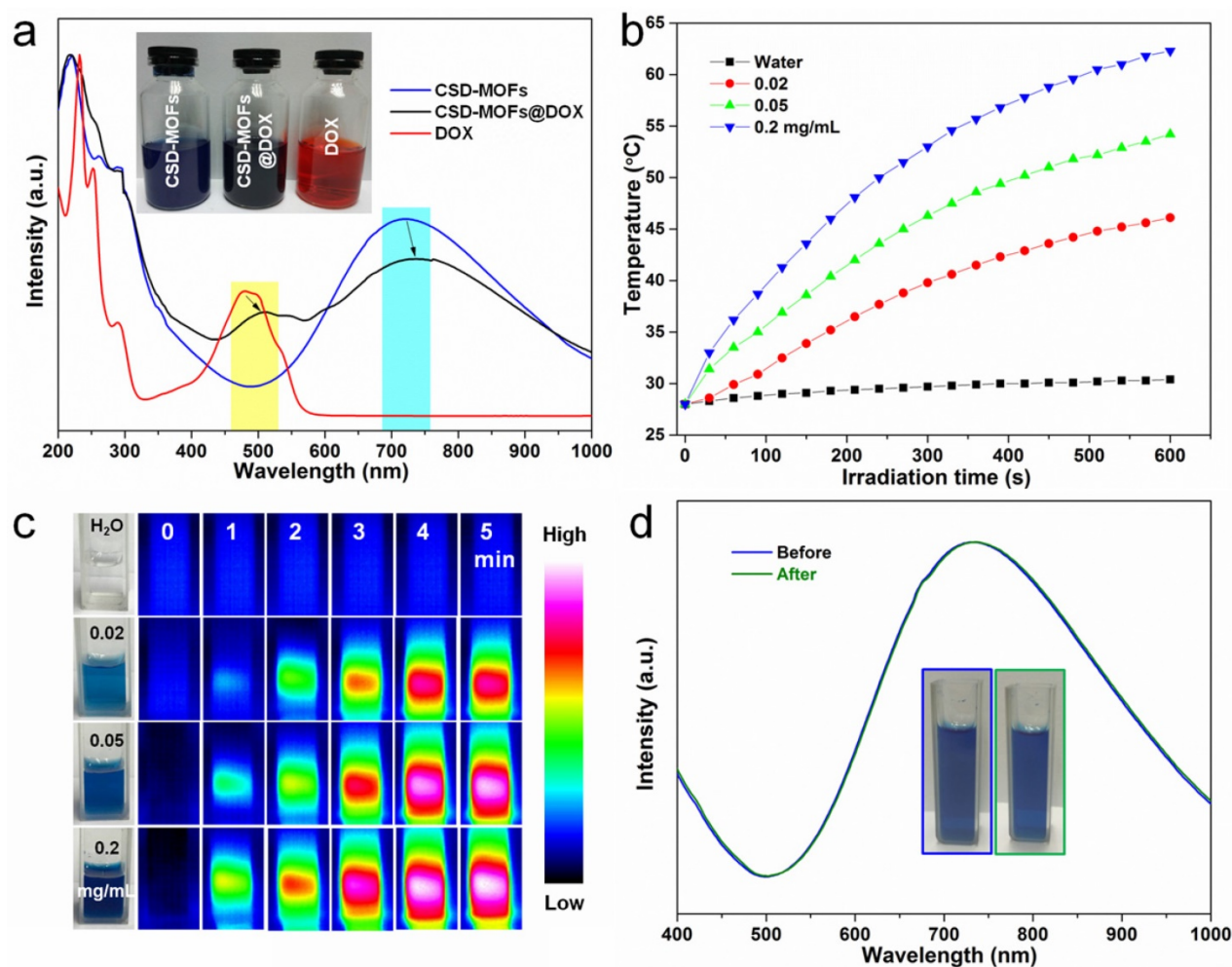


Figure 4. (a) UV-vis-NIR spectroscopy of CSD-MOFs, DOX and CSD-MOFs@DOX (inset: the representative photos of samples). (b) Heating curves of CSD-MOFs solutions of different concentrations under 808 nm NIR irradiation (1.6 W cm^{-2}). (c) Infrared thermal images of CSD-MOFs acquired within 5 min NIR irradiation. (d) UV-vis-NIR spectroscopy of CSD-MOFs before and after NIR irradiation.

FT-IR spectra were performed to demonstrate the successful loading of DOX (**Supplementary Figure S11**). Next, we studied the drug release behaviors of our CSD-MOFs@DOX. Cumulative release profiles were performed under buffers of different pH values (7.4, 6.2, and 5.0) and different temperatures (37 and 43.5 °C). Results showed that CSD-MOFs exhibit pH responsive DOX release property. Smallest release amount of DOX was observed at pH 7.4. With the reduction of pH value, the DOX release percentage increased. The accelerated release of DOX with the temperature increase from 37 °C to 43.5 °C should be attributed to the diffusion of the drug molecular under high temperatures (**Figure 5a**). We then wondered whether NIR-induced photothermal heating could also trigger drug release from nanoparticles. CSD-MOFs@DOX samples in pH 5.0 and 7.4 solutions were irradiated by the 808 nm laser (1.6 W cm^{-2} , 5 min) at different points. Compared with DOX released without laser irradiation, the DOX release with NIR-stimulus was

dramatically enhanced. Moreover, with same laser irradiation, the DOX release at the lower pH value (5.0) seemed to be more obvious compared to that physiological pH (7.4) (**Figure 5b**). The pH-responsive release profile is greatly beneficial to minimizing the side effects of chemotherapeutics and enhancing the antitumor efficiency considering the lower pH value in the microenvironment of tumor sites. The NIR-triggered drug release would be more effective once nanoparticles are internalized by tumor cells. TEM images were taken to further illustrate the degradation of the drug delivery system. Results indicated the morphology of the outer ZIF-8 suffers more obvious collapse under lower pH condition (**Figure 5c-e**).

Previous works indicated that Prussian blue analogues possess similar photoluminescence properties as carbon dots [11, 18]. Thus we wonder whether the CSD-MOFs would exhibit similar property. HeLa cells became brightly illuminated with multicolor images when they were excited with

403, 488nm single-photon laser and 750 nm two-photon laser pulses (Figure 6a). For subcellular localization, the HeLa cells were transfected with lysosomal-associated membrane protein mCherry-LAMP-1 and then incubated with CSD-MOFs for 24 h. Result showed that the green fluorescence from CSD-MOFs and the red fluorescence from mCherry-LAMP-1 are overlapped, demonstrating intracellular localization of CSD-MOFs are localized in endosomes/lysosomes. Besides, DOX is a fluorescent anticancer drug [49]. Herein, we also conducted *in vitro* fluorescence images of CSD-MOFs@DOX (Supplementary Figure S12). Results showed not only the blue and green fluorescence of CSD-MOFs but also the red fluorescence of DOX.

Due to its unique Fe(II)-C≡N-Fe(III) structure (Fe(II) is low spin ($S=0$) and Fe(III) is high spin ($S=5/2$)), Prussian blue nanoparticles can serve both T_1 and T_2 MR imaging contrast agent [50]. For *in vitro* test, serial dilutions were tested under a 3 T MR scanner and showed a concentration-dependent effect (Figure 6c, 6d). The r_1 and r_2 values of our CSD-MOFs nanocubes were measured to be $2.04 \text{ mM}^{-1} \text{ s}^{-1}$ and $22.87 \text{ mM}^{-1} \text{ s}^{-1}$, both of which are higher than that of PB nanoparticles ($r_1=0.314 \text{ mM}^{-1} \text{ s}^{-1}$, $r_2=15.50 \text{ mM}^{-1} \text{ s}^{-1}$) (Figure 6e, Supplementary Figure S13). The r_1 value of CSD-MOFs witnesses a remarkable enhancement

compared with pure PB. According to Solomon-Bloembergen-Morgan (SBM) theory, inner-sphere and outer-sphere mechanisms contribute to the paramagnetic relaxation enhancement of r_1 value of CSD-MOFs. The interaction between lattice water and Fe(II) highly affects the longitudinal relaxivity. Therefore, a well-known inner sphere T_1 relaxation of the inner PB and water molecules can be generated.

Subsequently, *in vivo* MR images were also conducted. T_1 - and T_2^* -weighted MR images of tumor at time points of pre-injection, 30 min, and 24 h post-injection of CSD-MOFs nanocubes were obtained (Figure 6f, 6g). Compared with the pre-injected imaged, both T_1 -weighted and T_2^* -weighted images of tumor exhibited enhanced signal at 24 h post-injection due to the enhanced permeability and retention effect (EPR) effect [51]. Herein, it should be noted that nanoparticles with large particle size ($>10 \text{ nm}$) are often cleared by the reticuloendothelial system (RES), especially through Kupffer cells [52-54]. As shown in Figure 6g, the MR signal of liver becomes darker, which suggests that liver is the major organ for the metabolism and clearance of the as-prepared CSD-MOFs, consistent with previous studies on T_2 MR imaging contrast agents [55, 56]. These results confirmed the high-performance of CSD-MOFs nanocubes as T_1/T_2 dual-modal contrast agent.

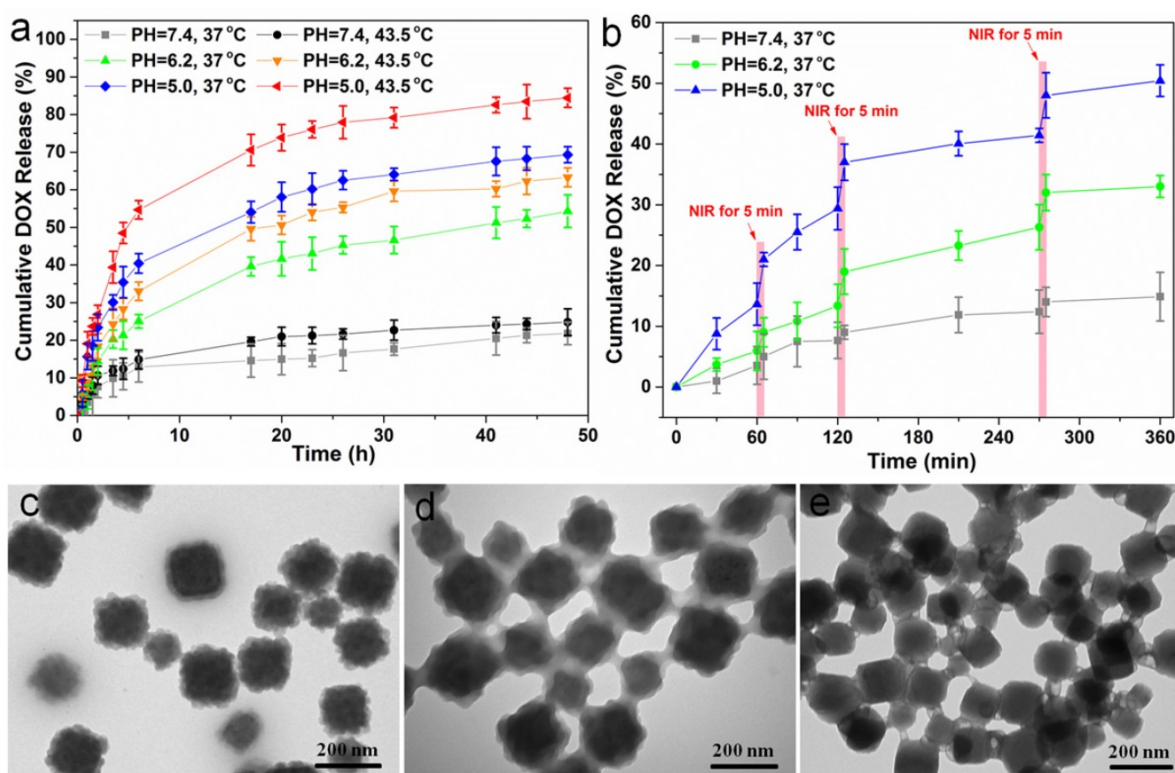


Figure 5. (a) DOX release from CSD-MOFs@DOX at different pH and temperature values. (b) NIR-triggered release of DOX. The samples were irradiated with an NIR laser (1.6 W cm^{-2}) for 5 min at different time points as indicated by the arrows. (c-e) TEM images of the DOX@CSD-MOFs after drug release at pH = 7.4, 6.2 and 5.0, respectively. Error bars were based on triplicated measurements.

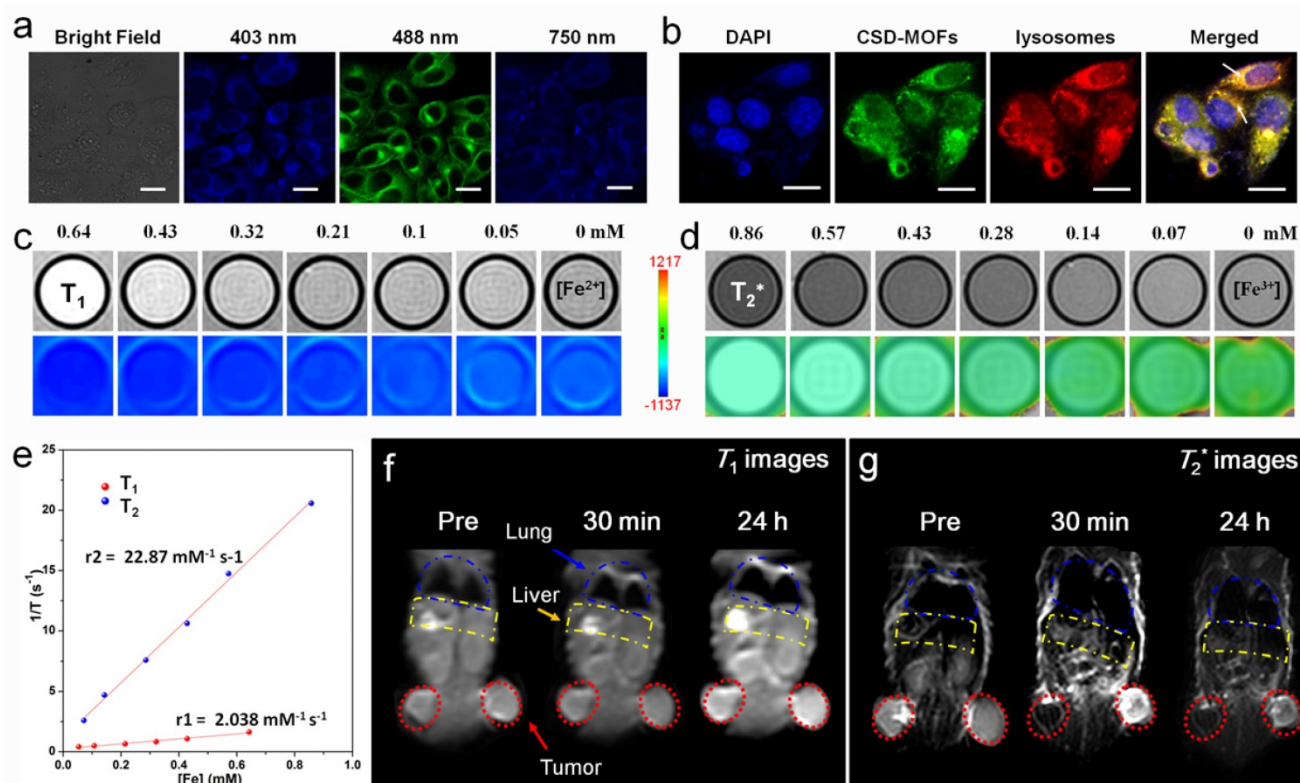


Figure 6. (a) CLSM images of HeLa cells under 403 nm, 488 nm single-photon and 750 nm two-photon excitation after incubation with CSD-MOFs. (b) CLSM image of HeLa cells stained with DAPI, mCherry-LAMP-1 and incubated with CSD-MOFs. (c) *In vitro* T_1 - and (d) T_2^* -weighted MR images of CSD-MOFs. (e) T_1 and T_2^* relaxation rates as a function of Fe concentration of CSD-MOFs nanoparticles. (f) *In vivo* T_1 - and (g) T_2^* -weighted MR images of HeLa tumor-bearing BALB/c mouse before, 30 min, and 24 h after intravenous injection of CSD-MOFs. (All scale bars: 20 μm).

Next, HeLa cells were adopted for testing the potential cytotoxicity of PB and CSD-MOFs. No obvious toxicity was observed at tested concentrations as evidenced by the standard methylthiazolyltetrazolium (MTT) assay (Figure 7a). Besides, the organic linker 2-MeIM also showed good biocompatibility at the tested concentrations (Figure S14). In addition, the hemolysis test showed that the no visible hemolytic effects were observed even at CSD-MOFs concentrations of 1000 $\mu\text{g mL}^{-1}$ in PBS, which is of great importance for CSD-MOFs via intravenous injection (Figure S15). For *in vitro* combination therapy, HeLa cancer cells were incubated with PBS, free DOX, CSD-MOFs, and CSD-MOFs@DOX with or without 808 nm laser at power density of 1.6 W cm^{-2} for 5 min. Although the cellular internalization of the nanocomplex was limited at the 4 h point, the CSD-MOFs@DOX treatment alone still shows cytotoxicity on HeLa cells which is due to the high delivering efficiency of CSD-MOFs. HeLa cells incubated with CSD-MOFs@DOX and then irradiated by NIR laser showed remarkably reduced viabilities (Figure 7b). However, the single chemotherapy group which treated with free DOX showed little cytotoxicity. On the other hand, the single photothermal effect by

CSD-MOFs, was also not as effective compared with the synergistic therapy. Our results demonstrated the enhanced cell killing synergistic effect by combined chemo-thermal therapy.

TEM images confirmed the intracellular uptake of the CSD-MOFs (Figure 7c). HeLa cells incubated with CSD-MOFs (50 $\mu\text{g mL}^{-1}$) for 24 h or 48 h were used for the observation of cellular uptake. For 48 h incubation, the outer ZIF-8 of most nanoparticles degraded while inner PB remained as residual particles, presumably due to partial dissolution of ZIF-8 particles. To directly witness the photothermal ablation ability, Calcein AM/PI staining was performed. Untreated group showed plenty of green color, which indicate they are live and healthy cells (Figure 7d). After being irradiated with NIR laser, an increasing area of red stained cells can be observed, especially after 10 min of laser irradiation.

Motivated by the outstanding photothermal conversion ability, we further evaluated the *in vivo* anticancer efficiency in detail. Before that, we first tested its blood circulation behavior after intravenous injection. The blood level of CSD-MOFs decreased gradually over time in accordance with a two-compartment model. The first $t_{1/2}$ and second $t_{1/2}'$ phase of circulation half-lives were calculated to be

0.4±0.05 h and 2.63±0.18 h, respectively (Figure 8a). HeLa tumor-bearing female nude mice were randomly divided into six groups with following treatments: (1) PBS, (2) NIR (808 nm for 5 min), (3) free DOX, (4) CSD-MOFs@DOX, (5) CSD-MOFs+NIR and (6) CSD-MOFs@DOX+NIR. Relative to the rapid tumor growth in the control group, statistically significant inhibition of tumor growth was observed

in the treatment groups (Figure 8b, Supplementary Figure S16). Compared to single Chemo-therapy (CSD-MOFs@DOX) and thermal-therapy (CSD-MOFs+NIR) could only slightly reduce the tumor growth (Figure 8c, 8d). Combination therapy of CSD-MOFs@DOX+NIR was found to be much more effective, demonstrating the synergistic anticancer effect (combination index, CI = 0.71).

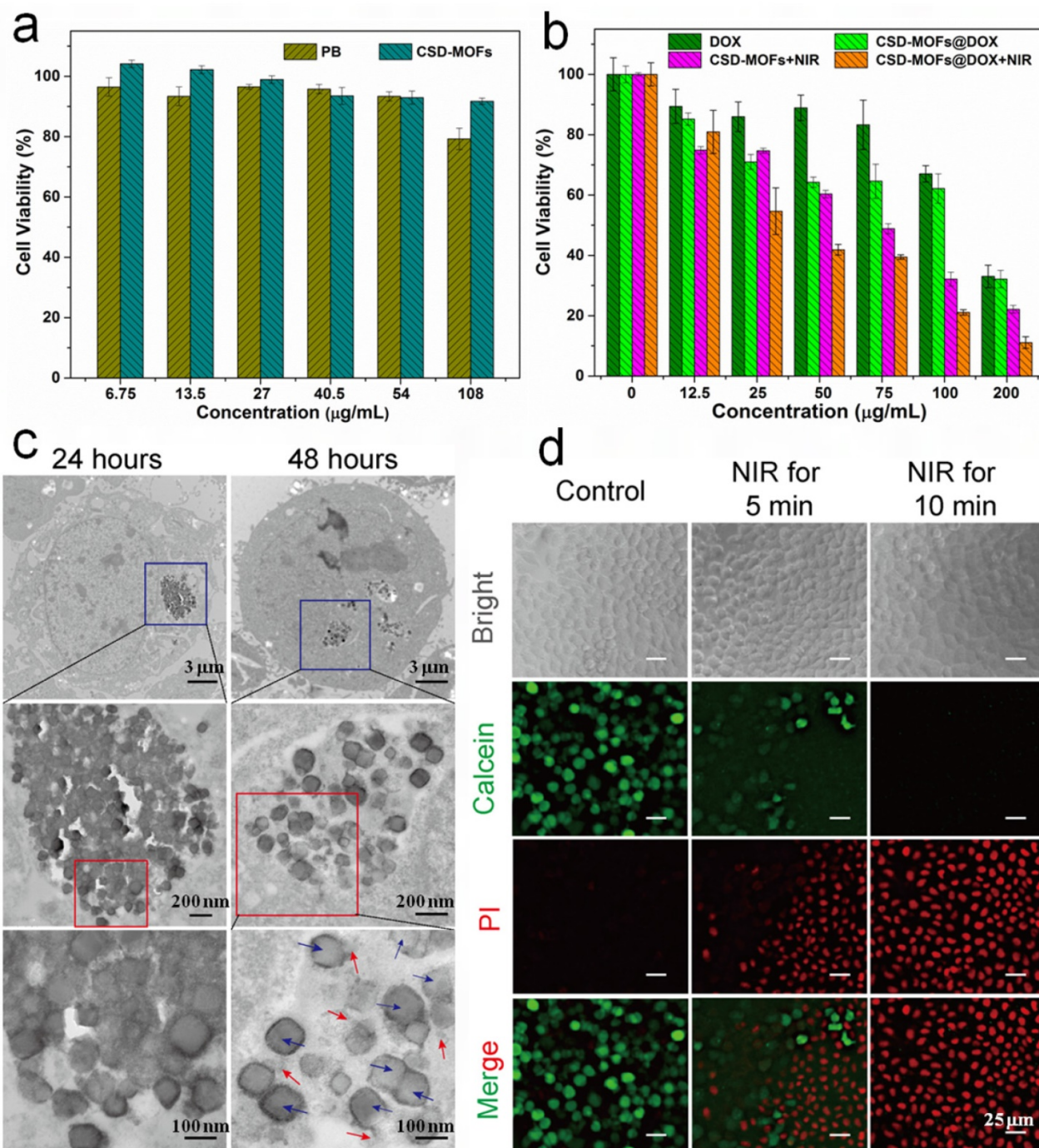


Figure 7. (a) Viability of HeLa cells incubated with PB and CSD-MOFs. (b) Relative viability of HeLa cells incubated with free DOX, CSD-MOFs@DOX, CSD-MOFs and CSD-MOFs@DOX with or without laser irradiation (1.6 W cm⁻², 5 min). (c) TEM images of HeLa cell after being incubated with CSD-MOFs for 24 h and 48 h (PB nanocubes (blue arrows) and ZIF-8 fragments (red arrows)). (d) HeLa cells incubated with CSD-MOFs suspension (50 µg/mL), and then subjected to 808 nm irradiation (Control; NIR for 5 min; NIR for 10 min with the Calcein channel or the PI channel) (All scale bars: 25 µm).

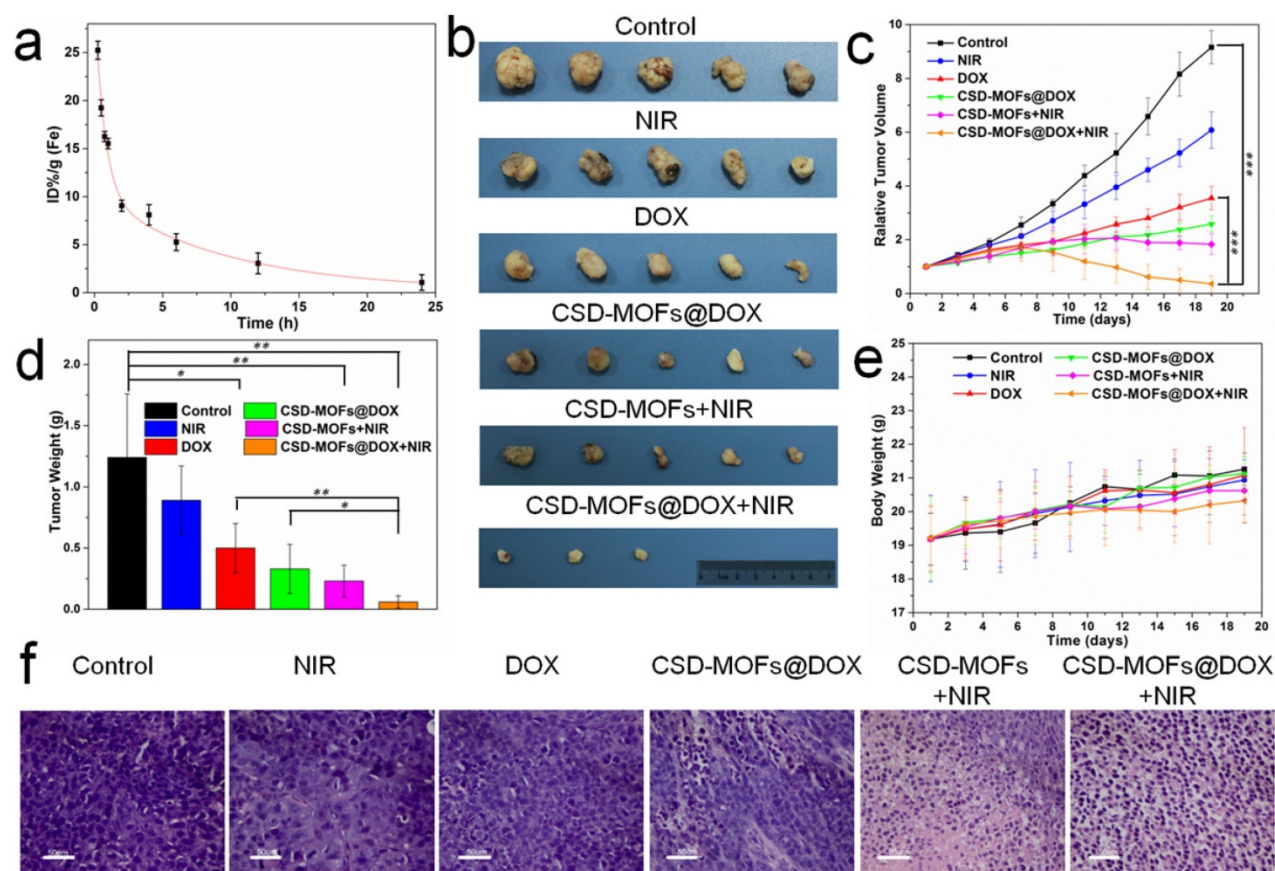


Figure 8. (a) Blood circulation of CSD-MOFs and the pharmacokinetics followed the two-compartment model. (b) Photographs of tumors harvested from mice receiving different therapeutic treatments. (c) Tumor growth curves of the corresponding group. (d) The tumors collected from all groups were weighted 19 days after various treatments. (e) Body weights of mice for varied time periods for 19 days. (f) Slices of tumor tissues stained with hematoxylin and eosin. (All the scale bar: 50 μ m) Statistical analysis was performed using the Student's two-tailed t-test (* p < 0.05, ** p < 0.01 and *** p < 0.001).

Afterwards, the slices of tumor were stained with hematoxylin and eosin (H&E) (Figure 8f). Evidently, the H&E images from CSD-MOFs+NIR and CSD-MOFs@DOX+NIR groups confirm that cancer cells have suffered serious damage, while other groups showed little or no changes. Considering Ki-67 index, tumor cell nuclei with homogenous granular staining, multiple speckled staining, or nucleolar staining were positively stained. The control group showed more Ki-67 positive index (Figure 9a) than other groups, which demonstrated that the tumors in control group suffering more rapid proliferation while CSD-MOFs@DOX+NIR can efficiently inhibit the proliferation.

In order to understand the metabolism and distribution of CSD-MOFs *in vivo*, HeLa tumor-bearing mice at 24 h post intravenous injection of CSD-MOFs was investigated with an ICP-AES method (Figure 9b). Results showed liver and spleen have a significant uptake of the particles, with an uptake of 0.22 g/kg in the liver and 0.08 g/kg in the spleen. To further evaluate the possible side effect, H&E stained slices of major organs were performed. There was no appreciable organ damage or

inflammation of the mice in all groups (Figure 9c, Supplementary Figure S17). And all groups showed the same body increase tendency as shown in Figure 8e. Those indicated that CSD-MOFs possess perfect biocompatibility. Besides, negligible aggregation or morphological changes was observed in the treated blood (Supplementary Figure S18). These results confirm the blood compatibility of the CSD-MOFs which is essential for *in vivo* drug delivery.

The CSD-MOFs have several unique features compared with other organic, inorganic theranostic platforms. (1) MOFs possess intrinsic large surface area and pore volume for drug loading. (2) CSD-MOFs integrate functionalities of two MOFs which cannot attainable from sole MOF source. (3) It shows both pH- (endogenous) and NIR- (exogenous) dual-stimuli responsive drug release profiles. (4) The usage of FOI and MRI imaging for *in vitro* and *in vivo* real-time drug release monitoring provide great potential for future precision medicine. (5) The excellent therapeutic effect and low cytotoxicity originated from the rapid pH-responsive combined therapy further allow it a promising theranostic agent for future clinical translation.

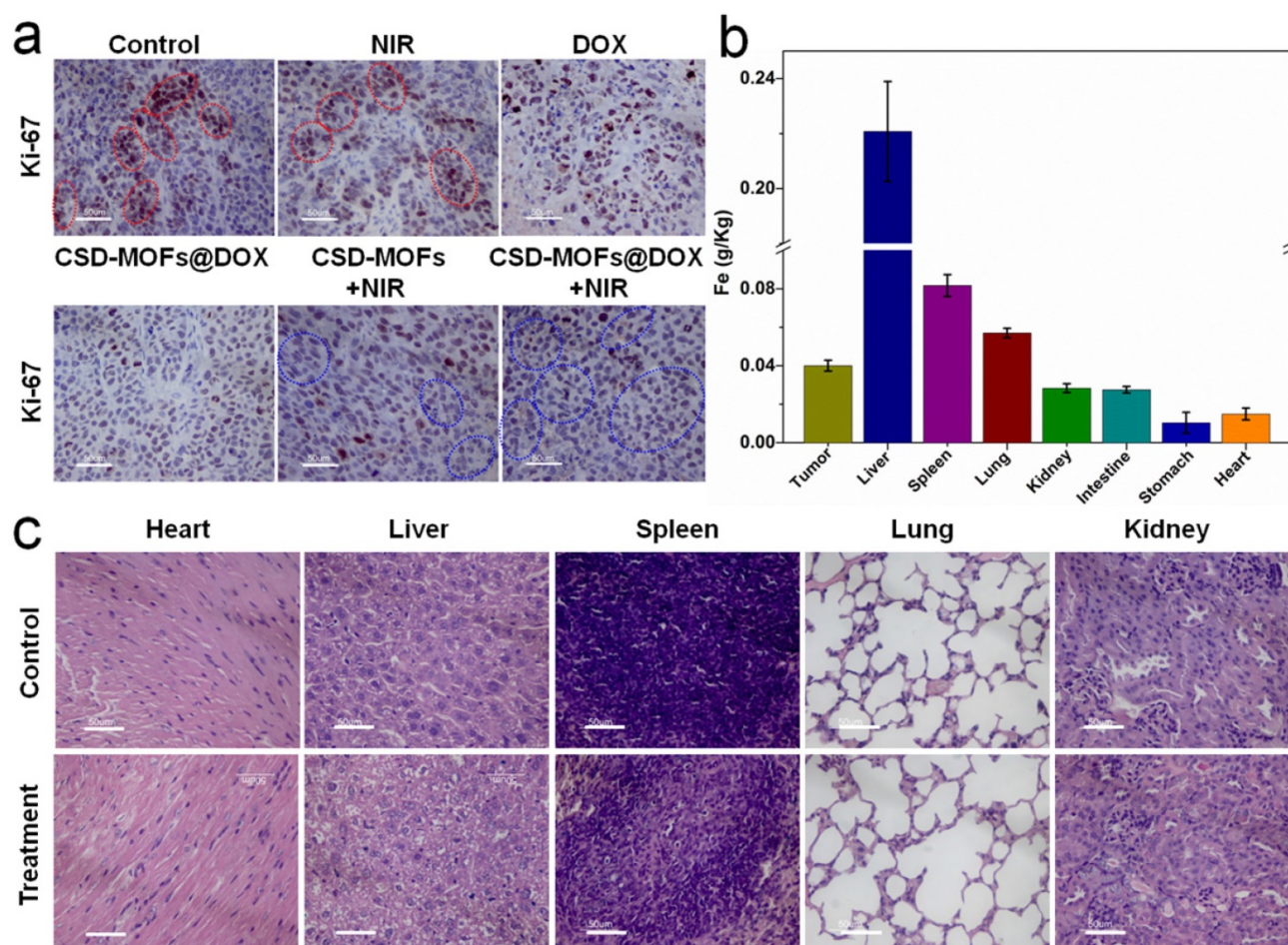


Figure 9. (a) Ki-67 stain of tumor sections collected from differently treated groups of mice. The brown nucleus (see those cells in red circles) indicated the proliferation of cells and the light blue nucleus (blue circles) indicated the inhibited proliferation of cells. (b) Biodistribution of Fe in the major organs of the HeLa tumor-bearing mice at 24 h post intravenous injection of CSD-MOFs. (c) H&E stained images of major organs of mice at 19th day. (All the scale bar: 50 μ m).

Conclusion

In conclusion, we developed novel CSD-MOFs by *in situ* growth of ZIF-8 MOFs shell on PB MOFs core to successfully achieve the *in vivo* synchronously diagnosis, synergistic chemo-thermal tumor therapy, and therapy monitoring by MRI/FOI dual mode imaging. Detailed investigation on the growth of ZIF-8 MOFs unveiled that there are two types of nucleation mechanism (homogeneous and heterogeneous) and the latter, which initiates the ZIF-8 formation on PB MOFs, can be promoted at lower precursor concentrations. The exceptionally high drug loading capacity, and sustained and effective pH-responsive drug release make core-shell CSD-MOFs an excellent drug carrier. We have shown that CSD-MOFs@DOX can be used as a promising pH- (endogenous) and NIR- (exogenous) dual-stimuli responsive drug delivery system. With the extremely high loading capacity of DOX and inherent excellent photothermal conversion property, the DOX-loaded CSD-MOFs present the distinct synergistic effect in

chemo-thermal tumor therapy. The *in vivo* results demonstrated that the synergistic tumor inhibition ratio ($V/V_0 = 0.62$) of CSD-MOFs@DOX+NIR is higher than that of other groups. Thus, CSD-MOFs is a promising theranostic platform derived from the heterogeneous hybridization of two biocompatible MOFs with different functionalities.

Experimental Section

Detailed experimental materials and methods can be found in the Supporting Information.

Supplementary Material

Experiment sections, supplementary figures and discussions. <http://www.thno.org/v07p4605s1.pdf>

Acknowledgments

We thank Z. B. Liu of Core Facility Center for Life Sciences of University of Science and Technology of China for imaging support. The work was supported by the National Natural Science Foundation of China, 21571168(Q. W. Chen), The

Most Grant 2016YFA0101202 (Z. Guo), U1232211 (Q. W. Chen), 31501130 (J. Zhou), CAS/SAFEA international partnership program for creative research teams and CAS Hefei Science Center (2016HSC-IU011).

Competing Interests

The authors have declared that no competing interest exists.

References

- Chen H, Zhang W, Zhu G, Xie J, Chen X. Rethinking cancer nanotheranostics. *Nat Rev Mater*. 2017; 2: 17024.
- Jain RK, Stylianopoulos T. Delivering nanomedicine to solid tumors. *Nat Rev Clin Oncol*. 2010; 7: 653-64.
- Gottesman MM. Mechanisms of Cancer Drug Resistance. *Annu Rev Med*. 2002; 53: 615-27.
- Chen W, Zhong P, Meng F, Cheng R, Deng C, Feijen J, et al. Redox and pH-responsive degradable micelles for dually activated intracellular anticancer drug release. *J Controlled Release*. 2013; 169: 171-9.
- Patel K, Angelos S, Dichtel WR, Coskun A, Yang Y-W, Zink JL, et al. Enzyme-Responsive Snap-Top Covered Silica Nanocontainers. *J Am Chem Soc*. 2008; 130: 2382-3.
- Ni D, Jiang D, Valdovinos HF, Ehlerding EB, Yu B, Barnhart TE, et al. Bioresponsive Polyoxometalate Cluster for Redox-Activated Photoacoustic Imaging-Guided Photothermal Cancer Therapy. *Nano Lett*. 2017; 17: 3282-9.
- Stuart MA, Huck WT, Genzer J, Muller M, Ober C, Stamm M, et al. Emerging applications of stimuli-responsive polymer materials. *Nat Mater*. 2010; 9: 101-13.
- Wang C, Xu H, Liang C, Liu Y, Li Z, Yang G, et al. Iron Oxide@Polypyrrole Nanoparticles as a Multifunctional Drug Carrier for Remotely Controlled Cancer Therapy with Synergistic Antitumor Effect. *ACS Nano*. 2013; 7: 6782-95.
- Chen J, Guo Z, Wang HB, Gong M, Kong XK, Xia P, et al. Multifunctional Fe₃O₄@C@Ag hybrid nanoparticles as dual modal imaging probes and near-infrared light-responsive drug delivery platform. *Biomaterials*. 2013; 34: 571-81.
- Dong Z, Gong H, Gao M, Zhu W, Sun X, Feng L, et al. Polydopamine Nanoparticles as a Versatile Molecular Loading Platform to Enable Imaging-guided Cancer Combination Therapy. *Theranostics*. 2016; 6: 1031-42.
- Wang D, Guo Z, Zhou J, Chen J, Zhao G, Chen R, et al. Novel Mn₃[Co(CN)₆]₂@SiO₂@Ag Core-Shell Nanocube: Enhanced Two-Photon Fluorescence and Magnetic Resonance Dual-Modal Imaging-Guided Photothermal and Chemo-therapy. *Small*. 2015; 11: 5956-67.
- Chen F, Hong H, Goel S, Graves SA, Orbay H, Ehlerding EB, et al. In Vivo Tumor Vasculature Targeting of CuS@MSN Based Theranostic Nanomedicine. *ACS Nano*. 2015; 9: 3926-34.
- Lin J, Wang S, Huang P, Wang Z, Chen S, Niu G, et al. Photosensitizer-Loaded Gold Vesicles with Strong Plasmonic Coupling Effect for Imaging-Guided Photothermal/Photodynamic Therapy. *ACS Nano*. 2013; 7: 5320-9.
- Verzijl JM, Joore HCA, van Dijk A, Wierckx FCJ, Jean Savelkoul TF, Glerum JH. In Vitro Cyanide Release of Four Prussian Blue Salts Used for the Treatment of Cesium Contaminated Persons. *J Toxicol Clin Toxicol*. 1993; 31: 553-62.
- Cheng L, Gong H, Zhu W, Liu J, Wang X, Liu G, et al. PEGylated Prussian blue nanocubes as a theranostic agent for simultaneous cancer imaging and photothermal therapy. *Biomaterials*. 2014; 35: 9844-52.
- Yang Y, Jing L, Li X, Lin L, Yue X, Dai Z. Hyaluronic Acid Conjugated Magnetic Prussian Blue@Quantum Dot Nanoparticles for Cancer Theranostics. *Theranostics*. 2017; 7: 466-81.
- Fu G, Liu W, Feng S, Yue X. Prussian blue nanoparticles operate as a new generation of photothermal ablation agents for cancer therapy. *Chem Commun (Camb)*. 2012; 48: 11567-9.
- Wang D, Zhou J, Chen R, Shi R, Zhao G, Xia G, et al. Controllable synthesis of dual-MOFs nanostructures for pH-responsive artemisinin delivery, magnetic resonance and optical dual-modal imaging-guided chemo/photothermal combinational cancer therapy. *Biomaterials*. 2016; 100: 27-40.
- Meneghini R. Iron Homeostasis, Oxidative Stress, and DNA Damage. *Free Radical Biol Med*. 1997; 23: 783-92.
- Valko M, Morris H, Cronin MTD. Metals, Toxicity and Oxidative Stress. *Curr Med Chem*. 2005; 12: 1161-208.
- Rosi NL, Eckert J, Eddaoudi M, Vodak DT, Kim J, O'Keeffe M, et al. Hydrogen Storage in Microporous Metal-Organic Frameworks. *Science*. 2003; 300: 1127-9.
- Yang S, Lin X, Lewis W, Suyetin M, Bichoutskaia E, Parker JE, et al. A partially interpenetrated metal-organic framework for selective hysteretic sorption of carbon dioxide. *Nat Mater*. 2012; 11: 710-6.
- Horcajada P, Gref R, Baati T, Allan PK, Maurin G, Couvreur P, et al. Metal-organic frameworks in biomedicine. *Chem Rev*. 2012; 112: 1232-68.
- He C, Liu D, Lin W. Nanomedicine Applications of Hybrid Nanomaterials Built from Metal-Ligand Coordination Bonds: Nanoscale Metal-Organic Frameworks and Nanoscale Coordination Polymers. *Chem Rev*. 2015; 115: 11079-108.
- Wang D, Zhou J, Chen R, Shi R, Wang C, Lu J, et al. Core-Shell Metal-Organic Frameworks as Fe²⁺ Suppliers for Fe²⁺-Mediated Cancer Therapy under Multimodality Imaging. *Chem Mater*. 2017; 29: 3477-89.
- Zheng H, Zhang Y, Liu L, Wan W, Guo P, Nystrom AM, et al. One-pot Synthesis of Metal-Organic Frameworks with Encapsulated Target Molecules and Their Applications for Controlled Drug Delivery. *J Am Chem Soc*. 2016; 138: 962-8.
- Ren H, Zhang L, An J, Wang T, Li L, Si X, et al. Polyacrylic acid@zeolitic imidazolate framework-8 nanoparticles with ultrahigh drug loading capability for pH-sensitive drug release. *Chem Commun (Camb)*. 2014; 50: 1000-2.
- Park KS, Ni Z, Cote AP, Choi JY, Huang RD, Uribe-Romo FJ, et al. Exceptional chemical and thermal stability of zeolitic imidazolate frameworks. *P Natl Acad Sci USA*. 2006; 103: 10186-91.
- Broadley MR, White PJ, Hammond JP, Zelko I, Lux A. Zinc in plants. *New Phytol*. 2007; 173: 677-702.
- Sun C-Y, Qin C, Wang X-L, Yang G-S, Shao K-Z, Lan Y-Q, et al. Zeolitic imidazolate framework-8 as efficient pH-sensitive drug delivery vehicle. *Dalton Trans*. 2012; 41: 6906-9.
- He M, Zhou J, Chen J, Zheng F, Wang D, Shi R, et al. Fe₃O₄@carbon@zeolitic imidazolate framework-8 nanoparticles as multifunctional pH-responsive drug delivery vehicles for tumor therapy in vivo. *J Mater Chem B*. 2015; 3: 9033-42.
- Zhuang J, Kuo CH, Chou LY, Liu DY, Weerapana E, Tsung CK. Optimized Metal-Organic-Framework Nanospheres for Drug Delivery: Evaluation of Small-Molecule Encapsulation. *ACS Nano*. 2014; 8: 2812-9.
- Miralda CM, Macias EE, Zhu M, Ratnasamy P, Carreon MA. Zeolitic Imidazole Framework-8 Catalysts in the Conversion of CO₂ to Chloropropene Carbonate. *ACS Catal*. 2012; 2: 180-3.
- Hong G, Antaris AL, Dai H. Near-infrared fluorophores for biomedical imaging. *Nature Biomedical Engineering*. 2017; 1: 0010.
- Huber PE, Jenne JW, Rastert R, Simiantonakis I, Sinn H-P, Strittmatter H-J, et al. A New Noninvasive Approach in Breast Cancer Therapy Using Magnetic Resonance Imaging-guided Focused Ultrasound Surgery. *Cancer Res*. 2001; 61: 8441-7.
- Liang X, Li Y, Li X, Jing L, Deng Z, Yue X, et al. PEGylated Polypyrrole Nanoparticles Conjugating Gadolinium Chelates for Dual-Modal MRI/Photoacoustic Imaging Guided Photothermal Therapy of Cancer. *Adv Funct Mater*. 2015; 25: 1451-62.
- Kumar R, Shin WS, Sunwoo K, Kim WY, Koo S, Bhuniya S, et al. Small conjugate-based theranostic agents: an encouraging approach for cancer therapy. *Chem Soc Rev*. 2015; 44: 6670-83.
- Chi C, Du Y, Ye J, Kou D, Qiu J, Wang J, et al. Intraoperative imaging-guided cancer surgery: from current fluorescence molecular imaging methods to future multi-modality imaging technology. *Theranostics*. 2014; 4: 1072-84.
- Zhao Z, Fan H, Zhou G, Bai H, Liang H, Wang R, et al. Activatable Fluorescence/MRI Bimodal Platform for Tumor Cell Imaging via MnO₂ Nanosheet-Aptamer Nanoprobe. *J Am Chem Soc*. 2014; 136: 11220-3.
- Song E, Han W, Li C, Cheng D, Li L, Liu L, et al. Hyaluronic Acid-Decorated Graphene Oxide Nanohybrids as Nanocarriers for Targeted and pH-Responsive Anticancer Drug Delivery. *ACS Appl Mater Interfaces*. 2014; 6: 11882-90.
- Yin W, Yan L, Yu J, Tian G, Zhou L, Zheng X, et al. High-Throughput Synthesis of Single-Layer MoS₂ Nanosheets as a Near-Infrared Photothermal-Triggered Drug Delivery for Effective Cancer Therapy. *ACS Nano*. 2014; 8: 6922-33.
- Lee J, Kim J, Kim WJ. Photothermally Controllable Cytosolic Drug Delivery Based On Core-Shell MoS₂-Porous Silica Nanoplates. *Chem Mater*. 2016; 28: 6417-24.
- Liu Y, Yang M, Zhang J, Zhi X, Li C, Zhang C, et al. Human Induced Pluripotent Stem Cells for Tumor Targeted Delivery of Gold Nanorods and Enhanced Photothermal Therapy. *ACS Nano*. 2016; 10: 2375-85.
- Zhang Z, Liu C, Bai J, Wu C, Xiao Y, Li Y, et al. Silver Nanoparticle Gated, Mesoporous Silica Coated Gold Nanorods (AuNR@MS@AgNPs): Low Premature Release and Multifunctional Cancer Theranostic Platform. *ACS Appl Mater Interfaces*. 2015; 7: 6211-9.
- Li M, Li L, Zhan C, Kohane DS. Core-Shell Nanostars for Multimodal Therapy and Imaging. *Theranostics*. 2016; 6: 2306-13.
- Hachula B, Nowak M, Kusz J. Crystal and Molecular Structure Analysis of 2-Methylimidazole. *J Chem Crystallogr*. 2010; 40: 201-6.
- Vasconcelos IB, Silva TGd, Militão CCG, Soares TA, Rodrigues NM, Rodrigues MO, et al. Cytotoxicity and slow release of the anti-cancer drug doxorubicin from ZIF-8. *RSC Adv*. 2012; 2: 9437.
- Cai X, Jia X, Gao W, Zhang K, Ma M, Wang S, et al. A Versatile Nanotheranostic Agent for Efficient Dual-Mode Imaging Guided Synergistic Chemo-Thermal Tumor Therapy. *Adv Funct Mater*. 2015; 25: 2520-9.
- Gao C, Lin Z, Jurado-Sanchez B, Lin X, Wu Z, He Q. Stem Cell Membrane-Coated Nanogels for Highly Efficient In Vivo Tumor Targeted Drug Delivery. *Small*. 2016; 12: 4056-62.
- Shokouhimehr M, Soehnlen ES, Hao J, Griswold M, Flask C, Fan X, et al. Dual purpose Prussian blue nanoparticles for cellular imaging and drug delivery: a

- new generation of T₁-weighted MRI contrast and small molecule delivery agents. *J Mater Chem*. 2010; 20: 5251.
51. Maeda H, Wu J, Sawa T, Matsumura Y, Hori K. Tumor vascular permeability and the EPR effect in macromolecular therapeutics: a review. *J Controlled Release*. 2000; 65: 271-84.
 52. Neuberger T, Schöpf B, Hofmann H, Hofmann M, Von Rechenberg B. Superparamagnetic nanoparticles for biomedical applications: Possibilities and limitations of a new drug delivery system. *J Magn Magn Mater*. 2005; 293: 483-96.
 53. Chouly C, Pouliquen D, Lucet I, Jeune JJ, Jallet P. Development of superparamagnetic nanoparticles for MRI: Effect of particle size, charge and surface nature on biodistribution. *J Microencapsulation*. 1996; 13: 245-55.
 54. Nel A, Xia T, Mädler L, Li N. Toxic Potential of Materials at the Nanolevel. *Science*. 2006; 311: 622-7.
 55. Chakravarty R, Valdovinos HF, Chen F, Lewis CM, Ellison PA, Luo H, et al. Intrinsically germanium-69-labeled iron oxide nanoparticles: synthesis and in-vivo dual-modality PET/MR imaging. *Adv Mater*. 2014; 26: 5119-23.
 56. Liu T, Shi S, Liang C, Shen S, Cheng L, Wang C, et al. Iron Oxide Decorated MoS₂ Nanosheets with Double PEGylation for Chelator-Free Radiolabeling and Multimodal Imaging Guided Photothermal Therapy. *ACS Nano*. 2015; 9: 950-60.